Noise Reduction Mechanisms due to Bio-Inspired Airfoil Designs

Andrew Bodling, Anupam Sharma

Noise Reduction Mechanisms due to Bio-Inspired Airfoil Designs

Andrew Bodling[1], Anupam Sharma[1]*

ISROMAC 2017

International Symposium on Transport Phenomena and Dynamics of Rotating Machinery

Maui, Hawaii

December 16-21, 2017

Abstract

This paper presents numerical analysis of an airfoil geometry inspired by the down coat of the night owl. The objective is to understand the mechanisms of airfoil trailing edge noise reduction that has been observed with such designs in previous experiments. The bioinspired geometry consists of an array of "fences" that are applied near the trailing edge of the NACA-0012 baseline airfoil. Wall-resolved large eddy simulations are performed over the baseline and the bioinspired airfoil geometries and the aeroacoustic performance of the two geometries are contrasted. Both models are simulated at chord-based Reynolds number $Re_c = 5 \times 10^5$, flow Mach number, $M_\infty = 0.2$, and angle of attack, $\alpha = 0°$. Farfield noise spectra comparisons between the baseline and the bioinspired airfoil near the airfoil trailing edge show reductions with the fences of up to 10 dB. The simulations reveal that the fences lift turbulence eddies away from the airfoil trailing (scattering) edge hence reducing scattering efficiency. These findings suggest that one of the mechanisms of noise reduction is the increased source-scattering edge separation distance.

Keywords

Aeroacoustics — Trailing Edge Noise — Large Eddy Simulations

[1] *Department of Aerospace Engineering, Iowa State University, Ames, IA, USA*

***Corresponding author**: sharma@iastate.edu

INTRODUCTION

One biological feature that has yet to be used in engineering innovations is the silent flight of nocturnal owls. One species of nocturnal owls - the barn owl (Tyto alba) - is particularly adept at silent flight. In this paper, we refer to the barn owl as 'the owl'. The owl has unique feather features – leading edge (LE) comb, downy coat on flight feathers, and trailing edge (TE) fringes, are collectively referred to as the "hush kit". There has been considerable research on using LE and TE features, modeled as serrations, to reduce airfoil noise [1, 2, 3]. The downy coat has been investigated analytically [4, 5] and experimentally [6, 7]. However, little to no numerical research investigating the acoustic impact of the owl down coat has been performed. This paper uses high-resolution large eddy simulations to investigate aerodynamic performance and perform diagnosis of sound sources in blade designs inspired by the down coat of the owl feathers

The particular bioinspired blade designs that form the focus of this paper were first discussed by Clark *et al.* [6]. They suggested that the down coat (made of hairs that rise up vertically and plateau in the flow direction) forms a canopy and makes the flow behave similar to forest canopy flows. They attempted to reproduce this canopy effect using "finlets" which were constructed in two different ways - (a) using an array of sharp edge fences, and (b) using tiny cylindrical rails. Clark *et al.* [6, 7] presented aeroacoustics measurements of trailing edge noise from airfoils with these finlets (fences and rails) installed using a substrate near the trailing edge of the baseline airfoil. The DU96-W-180 airfoil, commonly used in wind turbine applications, was selected as the baseline in the experiments [6, 7].

Figure 1 shows schematics of the two finlet designs used in the experiments. Plots (a) and (b) in the figure are the fence and rail configurations, respectively. Farfield sound measurements made using acoustic beamforming [8] showed that the finlet designs were significantly quieter than the baseline airfoil [7].

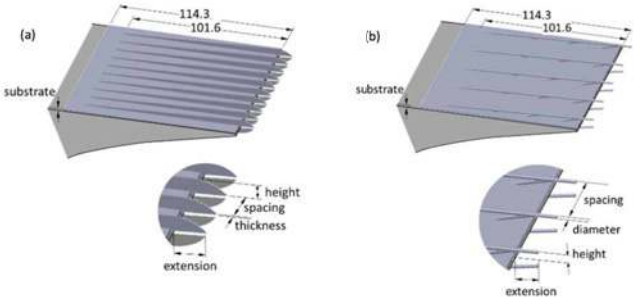

Figure 1. Schematics of two finlet designs used by Clark *et al.* [7].

This paper presents results of highly-resolved large eddy simulations of a baseline airfoil as well as the baseline airfoil fitted with two different finlet fences designs. The baseline airfoil used in this study is NACA-0012, which is different from the experiments of Ref. [7]. Furthermore, the simulations are performed at a much smaller Reynolds number compared to the experiments – $Re_c = 5 \times 10^5$ versus 2.1×10^6.

These simplifications are made to manage the computational complexity of the problem. Nevertheless, the simulations reveal several interesting flow physics that shed new light on the potential mechanisms of the observed noise reduction, thus supplementing the experimental results of Ref. [7]. This research builds upon authors' previous studies in simulating finlet fences [9, 10]. In this article, we focus on the aeroacoustic impact of the geometry of the leading edge of the finlet fences. Results from three sets of simulations are presented and compared: (a) baseline airfoil (NACA-0012), and the baseline airfoil with finlet fences installed where the leading edge of the fence is modeled as a (b) single step, and (c) as a stair step. Figure 2 contrasts the geometries of the fences used in the experiments with those used in the simulations.

In the experiments, the leading edge of the fence is nearly parallel to the flow while in the "single-step" simulation, the leading edge is orthogonal to the flow. This difference in the fence geometry between the experiments and the single-step simulation has important aeroacoustic consequences. Potential problems with the orthogonal leading edge in the single-step simulation, as identified in Ref. [10], include scattering of boundary layer turbulence into radiated sound, and production of turbulence at the sharp edge. To alleviate this problem and to better match the experimental geometry, the fence is modeled using a "stair-step" geometry in this paper. While the simulated stair-step geometry is still an approximation to the smooth edge in the experiments, the smaller vertical jumps are de-correlated by spatial separation and hence not as efficient in acoustic scattering.

The objective is to make *qualitative* comparisons between the simulations and experiments with the stair-step leading edge fence geometry to gain confidence in the simulations, and then perform source diagnostics using the highly-resolved flowfield to enhance understanding of the noise reduction mechanisms of finlets.

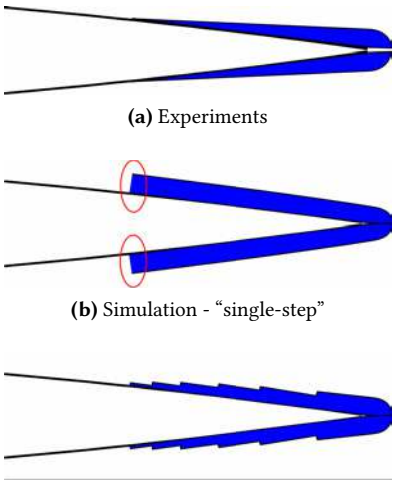

(a) Experiments

(b) Simulation - "single-step"

(c) Simulation - "stair-step"

Figure 2. Schematics highlighting the differences in fence geometries between the experiments and the two sets of simulations presented in this work.

1. NUMERICAL METHODOLOGY

A two-step approach is used for noise prediction. Fluid flow simulations are first carried out using a computational fluid dynamics (CFD) solver and subsequently, an integral method (acoustic analogy) is used with the CFD data to compute the radiated noise in the far-field. The compressible Navier-Stokes solver, FDL3DI [11] is used for the fluid flow simulations. The numerical approach used here has been previously validated by the authors and utilized to assess noise reduction ability of leading edge serrations [3]. Brief descriptions of the flow solver and the noise radiation solver are provided below for completeness.

The compressible Navier-Stokes solver, FDL3DI [11], is used for the fluid flow simulations. The governing fluid flow equations (solved by FDL3DI), after performing a time-invariant curvilinear coordinate transform $(x, y, z) \rightarrow (\xi, \eta, \zeta)$, are written in a strong conservation form as

$$\frac{\partial}{\partial t}\left(\frac{\mathbf{U}}{J}\right)+\frac{\partial \hat{\mathbf{F}}_I}{\partial \xi}+\frac{\partial \hat{\mathbf{G}}_I}{\partial \eta}+\frac{\partial \hat{\mathbf{H}}_I}{\partial \zeta} = \frac{1}{Re}\left[\frac{\partial \hat{\mathbf{F}}_v}{\partial \xi}+\frac{\partial \hat{\mathbf{G}}_v}{\partial \eta}+\frac{\partial \hat{\mathbf{H}}_v}{\partial \zeta}\right], \quad (1)$$

where J is the Jacobian of the coordinate transformation, $\mathbf{U} = \{\rho, \rho u, \rho v, \rho w, \rho E\}$; the expressions for inviscid flux terms, $\hat{\mathbf{F}}_I, \hat{\mathbf{G}}_I, \hat{\mathbf{H}}_I$ and viscous flux terms, $\hat{\mathbf{F}}_v, \hat{\mathbf{G}}_v, \hat{\mathbf{H}}_v$ are provided in Ref. [11]. We perform 'implicit' LES (ILES) simulations using FDL3DI by employing sixth-order spatial accuracy, eighth-order low pass filters, and a second order, implicit time integration scheme.

Far-field sound propagation is performed using the Ffowcs Williams-Hawkings (FW-H) acoustic analogy [12]. By neglecting volume sources (non-negligible only at very high flow speeds), the following integral equation is obtained for far-field acoustic pressure, p' at location $\mathbf{x}$ and time t:

$$p'(\boldsymbol{x},t) = \frac{1}{4\pi\,|1-M_r|\,|\boldsymbol{x}|}\left(\frac{\partial}{\partial t}\iint [\rho_0 u_i n_i + \rho'(u_i - U_i)n_i]\mathrm{d}\Sigma + \frac{x_i}{c\,|\boldsymbol{x}|}\frac{\partial}{\partial t}\iint [p' n_i + \rho u_i(u_j - U_j)n_j]\mathrm{d}\Sigma\right), \quad (2)$$

Solving Eq. 2 requires integrating over a surface Σ that encloses all sound sources. In the above, n_i is normal to the surface Σ, p' and ρ' are pressure and density fluctuations, ρ_0 is mean density, u_i' is perturbation flow velocity and U_i is the velocity of the surface Σ. The source is at the origin, and $\boldsymbol{x}$ denotes the observer location. We choose a "porous" surface around the airfoil defined by one of the gridlines (ξ = constant > 1; $\xi = 1$ is the airfoil surface) of the innermost grid block. The FW-H solver has been validated previously against canonical problems (point monopole, dipole, and quadrupole) as well as against experimental data for aerodynamic noise from propellers [13].

2. GEOMETRY MODELING, MESHING, AND BOUNDARY CONDITIONS

The NACA-0012 airfoil is selected as the baseline airfoil. For the bioinspired airfoil, finlet fences are added near the airfoil trailing edge. The span length of the airfoil model in the simulations is 5.85% of the airfoil chord. A single-block, O-grid is used to generate a 2-D mesh around the baseline airfoil, which is repeated in the span direction to obtain the 3-D grid. The O-grid in the physical space (x, y, z) maps to an H-grid in the computational domain (ξ, η, ζ). The following orientation is used: $\hat{\boldsymbol{e}}_\xi$ points radially out, $\hat{\boldsymbol{e}}_\eta$ is in the circumferential direction. $\hat{\boldsymbol{e}}_\zeta$ is along the span direction such that the right hand rule, $\hat{\boldsymbol{e}}_\zeta = \hat{\boldsymbol{e}}_\xi \times \hat{\boldsymbol{e}}_\eta$ is obeyed. The mesh density of the baseline grid used in this study is similar to that described in Ref. [14], which was a LES of flow over an airfoil at $Re_c = 5\times10^5$. Detailed results of a grid independence study for that problem are available in Ref. [15].

Periodicity is imposed in the span direction ($\hat{\boldsymbol{e}}_\zeta$). Periodic boundary conditions are implemented using the Overset grid approach in FDL3DI. A minimum of five-point overlap is required by FDL3DI to ensure high-order accurate interpolation between individual meshes. The airfoil surface is modeled as a no-slip, adiabatic wall. Freestream conditions are prescribed at the outer boundary and the grid is coarsened away from the airfoil surface in order for the filtering procedure to dissipate all perturbations from the flow before they reach the outer boundary.

2.1 Baseline Airfoil Mesh

The baseline is the NACA-0012 airfoil with a rounded trailing edge. The simulations are carried out at chord-based Reynolds number, $Re_c = 5 \times 10^5$, angle of attack, $\alpha = 0°$, and flow Mach number, $M_\infty = 0.2$. The choice of the first cell height with these flow conditions gives an average y^+ of 0.567 for the baseline geometry. The turbulent boundary layer is highly resolved. As an example, the boundary layer at $x/c = 0.85$ contains 110 grid points with approximately 15 points in the viscous sublayer. The max grid stretching ratio at the top of the boundary layer is 1.04. Figure 3 shows close-up, cross-sectional views of the baseline O-grid. For clarity, every fourth point in the radial and circumferential direction is shown in Fig. 3. Table 1 provides grid metrics averaged over the turbulent flow region of the baseline simulation. The metrics are also averaged along the span.

Table 1. Baseline grid metrics

$N_\xi \times N_\eta \times N_\zeta$	y^+ avg, max	x^+ avg, max	z^+ avg, max
$410 \times 1937 \times 101$	0.567, 0.665	28.7, 37.1	14.9, 17.3

2.2 Finlet Fence Geometry and Mesh

The meshes for the one-step and stair-step fence simulations are obtained from the baseline mesh by performing *hole-cutting* (also called point-blanking). Hole-cutting involves removing mesh points that represents the interior of a solid. In the simulations presented in this work, the regions occupied by the fences (defined by specifying ranges $\xi_1 - \xi_2$, $\eta_1 - \eta_2$, and $\zeta_1 - \zeta_2$) are cut out from the baseline grid and the no-slip condition is applied to the new boundaries thus created. The PEGASUS software [16] is used to perform hole-cutting.

Figure 4 shows cross-sectional views of the single-step and stair-step finlet fence meshes; the views are zoomed in on the fence region to clearly show the geometry differences. The red regions represent the grid points that are removed from the calculation by FDL3DI. Figure 5 shows top views of the baseline mesh and the single-step fence mesh. The red lines are the no-slip boundaries. The stair-step mesh is modeled in the same way except the height of the fence is varied in discrete steps with distance along the chord. The effect of not refining the mesh in the z-direction is assumed to be negligible since near the fence walls the max z^+ is approximately 30.6, which is not significantly greater than the baseline z^+ value.

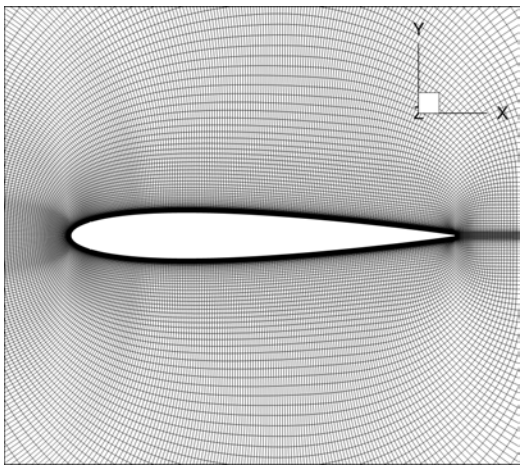

(a) Baseline mesh

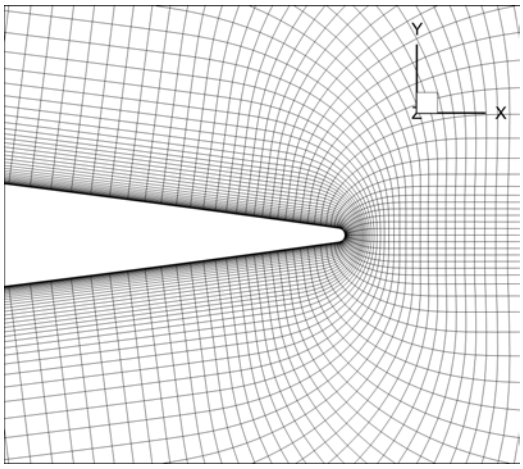

(b) Baseline mesh near the TE

Figure 3. O-grid topology of the baseline mesh used in the simulation. The trailing edge is rounded and the mesh near the TE is shown in (b). Every fourth point along each axis is shown for clarity.

A mesh containing a single fence element is created and then repeated six times along the span to obtain a 3-D mesh with a span of 5.85% chord. The dimensions (height and spacing) of the two finlet fence geometries simulated are similar to configuration 13 in the experiments of Ref. [7], with the exception of the LE shape. The leading edge of the fence is at $x/c = 0.875$. The height of the single-step fence (H), at the front of the fence is about 75% of the boundary layer thickness ($y^+ \sim 130$). The spacing of the fences is $1.5 \times H$ and the thickness of the fences is $0.085 \times H$. It should be emphasized that other than the holes (point blanking) introduced in the fence meshes, the grids for all three cases (baseline and two fences) are identical. This eliminates grid-to-grid differences in the simulation results when comparing the different designs.

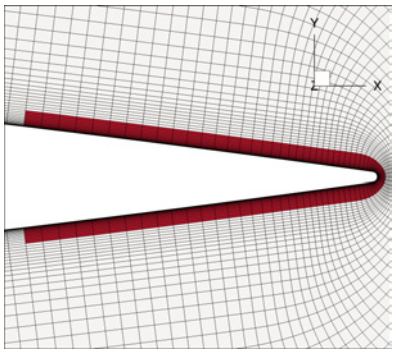

(a) Single-step fence mesh

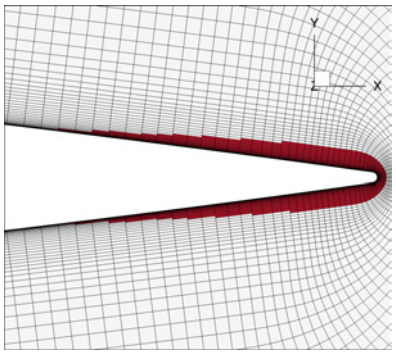

(b) Stair-step fence mesh

Figure 4. Cross-sectional (zoom) views of the computational meshes used to simulate the single-step and stair-step fence geometries. Every fourth grid point along each axis is shown for clarity.

3. RESULTS

This section presents the baseline validation and aeroacoustics results of the numerical simulations followed by a discussion on noise reduction mechanisms with the fence finlet designs.

3.1 Boundary Layer Trip

Since the simulation Re_c ($= 5 \times 10^5$) is much smaller than that of the experiments ($\approx 2 \times 10^6$), the boundary layer on the airfoil surface is tripped in the simulations. It should be noted that the boundary layer was also tripped in the experiments using a serrated tape. In the simulations, boundary layer tripping is achieved by placing a geometry-resolved "trip wire" at $x/c = 0.05$, measured from the leading edge of the airfoil. The trip wire successfully forces the boundary layer to transition well upstream, compared to where it would otherwise transition naturally, thereby achieving a turbulent boundary layer similar to what would occur via natural transition at high Re_c. Details of the tripping methodology are available in Ref. [10].

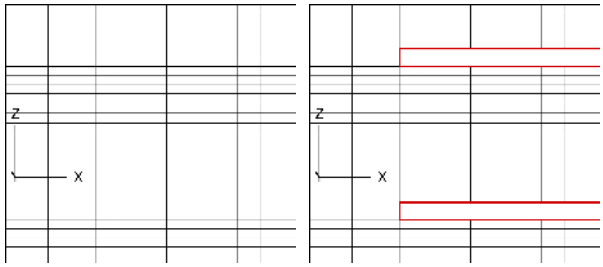

(a) Baseline **(b)** Single-step fence

Figure 5. Top views of the baseline and single-step fence meshes. Each fence element is modeled to be two cells thick in the simulations.

3.2 Baseline Validation

Once the transients are removed from the 3-D simulations, the simulation data is averaged in time for approximately 2.5τ with 63,000 samples to obtain aerodynamic performance predictions; $\tau = tu_\infty/c$ is the characteristic flow time, where c is airfoil chord, t is the dimensional time, and u_∞ is the freestream flow speed. Time-averaged flow data is further averaged in span and compared against experiments as well as against XFOIL results. Validations of the C_p and C_f distributions of the baseline simulation with experimental data and XFOIL predictions are documented in Ref. [10].

Figure 6 compares the baseline span-averaged normalized velocity profile, U^+, for different chord locations on the upper side of the airfoil from $x/c = 0.58$ to $x/c = 0.95$. The viscous sublayer is well resolved. The slope in the log-law region is found to be 1/0.34, which is slightly different than the value of 1/0.41 obtained with the von Kármán constant. Experiments by Lee and Kang [17] for turbulent flow over a NACA 0012 airfoil at $Re_c = 600,000$ found the slope to be closer to 1/0.34 (see Fig. 6).

Figure 7 shows comparisons of the normalized Reynolds stresses for the baseline airfoil as computed using the FDL3DI simulations presented here, DNS of a turbulent boundary layer with an adverse pressure gradient from Spalart and Watmuff [18], and a LES of a NACA 0012 at $Re = 4 \times 10^5$ and $\alpha = 0°$ from Wolf and Lele [19]. In the DNS, the Reynolds number based on the x coordinate in the flow direction is $Re_x = 3.4 \times 10^5$. The pressure gradient parameter ($\beta = (\delta^*/\tau_w)\mathrm{d}p/\mathrm{d}x$), varies from 0.0 to 2.0 in the x direction, where

the Reynolds stresses are at an x location corresponding to $\beta = 1$. The data from Ref. [19] and the current LES has a $\beta \approx 1$ at $x/c = 0.85$. Aside from the $\overline{u_1u_1}$ peak near the wall in the DNS, good agreement is seen with the DNS results of Ref. [18] and LES results of Ref. [19].

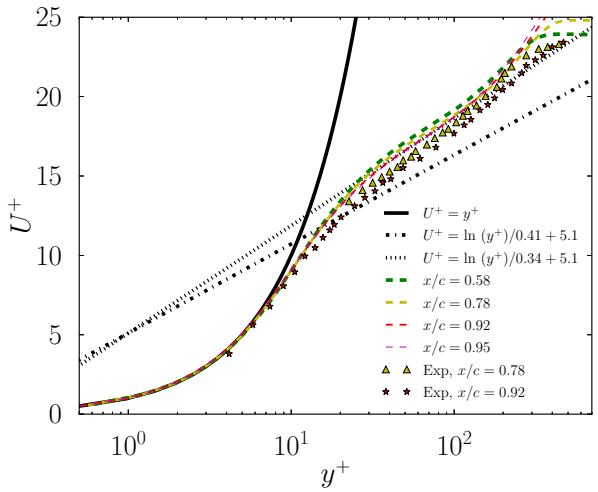

Figure 6. Baseline mean velocity profiles normalized by friction velocity plotted in wall units at different chord locations. Measurements are from Lee and Kang [17].

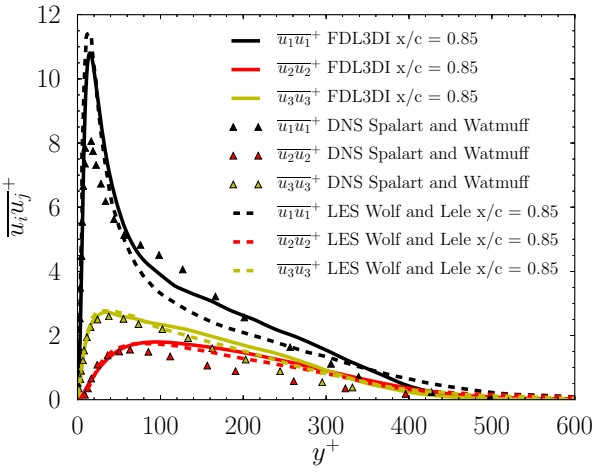

Figure 7. Comparison of FDL3DI predictions of normalized Reynolds stresses for the baseline airfoil with DNS results of a turbulent boundary layer in an adverse pressure gradient from Spalart and Watmuff [18], and a LES of a NACA 0012 at $Re = 4 \times 10^5, \alpha = 0°$ from Wolf and Lele [19].

Coherence squared, γ^2, between two points $\mathbf{x}$ and $\mathbf{y}$ is defined as

$$\gamma^2_{xy}(\omega) = \frac{|S_{xy}(\omega)|^2}{S_{xx}(\omega)S_{yy}(\omega)}, \tag{3}$$

where $S_{xx}(\omega)$ is pressure spectral density, $S_{pp}(\omega)$ evaluated at point $\mathbf{x}$ and $S_{yy}(w)$ is $S_{pp}(\omega)$ evaluated at point $\mathbf{y}$, where $\mathbf{x}$ and $\mathbf{y}$ are points at a given chordwise location but separated in the spanwise direction. The coherence function is often used to access whether the span length is long enough for a LES so that all sources of sound radiate sound independently. For the baseline simulation, $\gamma^2_{xy}(\omega)$ is computed using Eq. 3 using 7τ of data with 2000 samples divided into 20 segments with 50% overlap (Welch's method). Figure 8 compares $\gamma^2_{xy}(\omega)$ at different chordwise locations along the airfoil and frequencies. $\gamma^2_{xy}(\omega)$ is seen to decay to near zero for all frequencies at all chordwise locations.

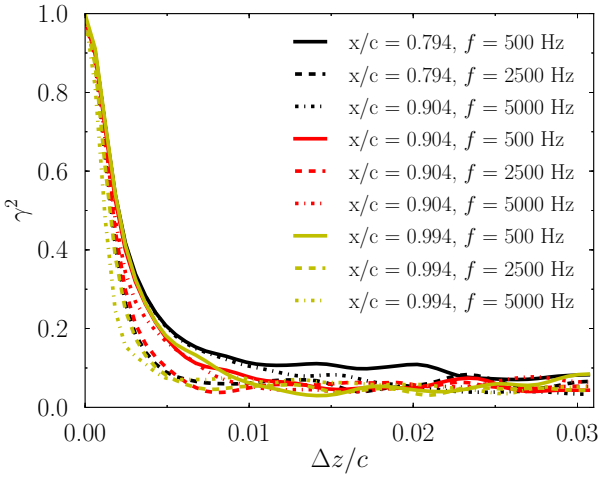

Figure 8. Spanwise coherence squared (γ^2) on the upper surface of the baseline airfoil at $x/c = 0.794$, 904, and 0.994 for $f = 500$, 2500 and 5000 Hz.

3.3 Surface Pressure Spectra

The primary noise generation mechanism in this low Mach number flow is the scattering into radiating sound of the hydrodynamic energy in the boundary layer turbulence by the airfoil trailing edge. Unsteady surface pressure near the trailing edge is therefore a measure of noise source strength. Surface pressure spectra are computed at $x/c = 0.998$. Numerical data is collected for approximately 5τ. Welch's method is used with 1400 samples divided into 20 segments to reduce scatter in the spectra. The spectra are also averaged over the span. The points that lie within the fences (which are not solved by FDL3DI) are removed in the averaging procedure for the fence simulation.

Figure 9 (a) compares the predicted spectra from the three simulations. Compared to the baseline, a measurable reduction at high frequencies and a small increase at low frequencies are observed in the predicted surface pressure spectra with both the single-step and stair-step fence geometry. These observations are compared *qualitatively* with the measured surface pressure spectrum from Ref. [20] (Fig. 9 (b)). The figures show that the predictions agree qualitatively with the measurements – reduction is observed at high frequencies which an increase in spectral magnitude is observed at low frequencies. Interestingly, the surface pressure reductions are found to be insensitive to the leading edge geometry

of the fence.

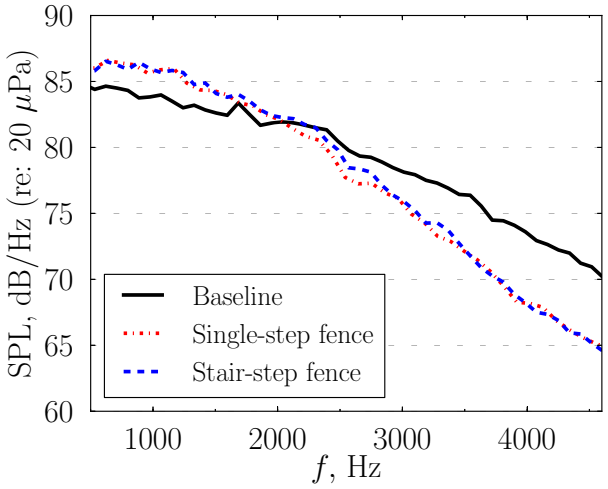

(a) FDL3DI predicted surface pressure spectra

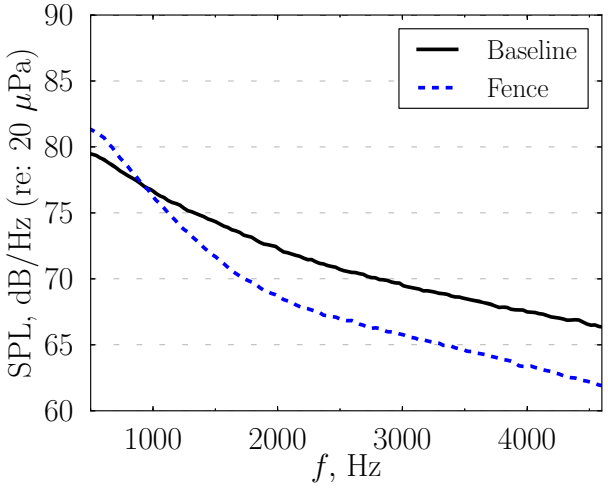

(b) Measured surface pressure spectra

Figure 9. Qualitative comparison between the predicted and measured surface pressure spectra at the trailing edge $x/c = 0.998$. Measurements are from Ref. [20].

3.4 Far field Aeroacoustics

Fluid dilatation ($|\boldsymbol{\nabla}.\boldsymbol{v}|$) is representative of instantaneous acoustic perturbations. Figure 10 shows the dilatation field for the baseline simulation, where the broadband noise from the airfoil trailing edge can be seen. A clear tonal noise signature is visible in the simulation, which emanates from the trip wire located on the airfoil surface at $x/c = 0.05$. The tonal noise signature from the trip wire is present in all three simulations. Vorticity contours near the trip wire are shown in Fig. 11. The contour plot shows the flapping shear layer behind the trip wire that causes the extraneous noise. While this noise source is undesirable in the simulations, the frequency of this tone is much higher than the broadband noise frequencies of interest. In a linearized acoustics sense, the effect of this extraneous tone on relevant broadband noise spectrum is ignored in the current predictions.

The in-house FW-H solver is used to calculate the far field noise. For the baseline airfoil, the integration (Kirchoff) surface can be selected as the airfoil surface. However, for the fence geometries, the FW-H surface will have to include the walls of each fence to ensure that noise contributions from all surfaces are included. Sampling data at the fence surfaces is quite tedious as they cannot be defined as constant ξ, η, or ζ boundaries. A permeable surface is therefore selected that includes the fences and the airfoil. Furthermore, the location of the permeable FW-H surface (marked with the red curve in Fig. 10) is chosen so that it is outside the undesired, high-frequency waves emanating from the trip wire. The integration surface extends from $-0.6 < x/c < 1.6$ and $-0.5 < y/c < 0.5$. Although the surface is not close to the airfoil, the grid is stretched very slowly up to the integration surface (stretching ratio < 1.06 near the FW-H surface). Therefore, the amount of numerical dissipation in the frequencies of interest is expected to be small.

Figure 12 shows the predicted far field noise for the baseline and the two fences at an azimuth angle of $\theta = 90°$ (see angle in Fig. 10). The spectra is computed from 1200 samples ($\approx 4\tau$), divided into 13 segments for spectral averaging. The azimuth angle is measured from downstream, and is positive in the counter-clockwise direction. Commensurate with the observed reductions in surface pressure spectra, the stair-step fence yields a substantial reduction in farfield noise compared to the baseline between 500 Hz – 5 kHz. However, despite similar reductions in surface pressure spectra for the single-step fence, no reduction is observed in the far field noise in the single-step simulation. We hypothesize that the orthogonal leading edge in the single-step simulation is offsetting the benefit of the fences.

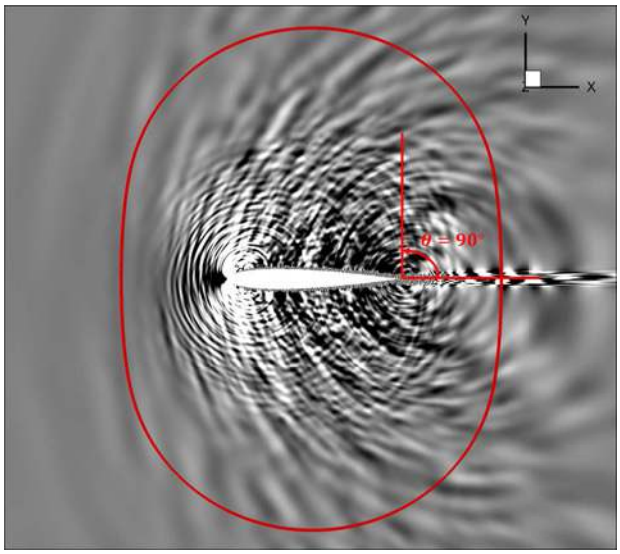

Figure 10. Fluid dilatation contours for the baseline simulation. The integration surface used is noted with the red curve. Observer angle (θ) is measured from downstream.

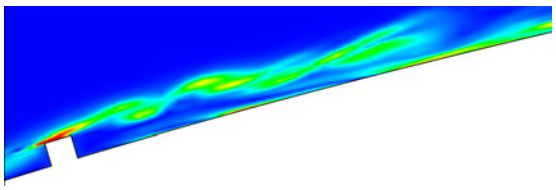

Figure 11. Shear layer behind the trip wire for the baseline simulation shown using vorticity magnitude contours.

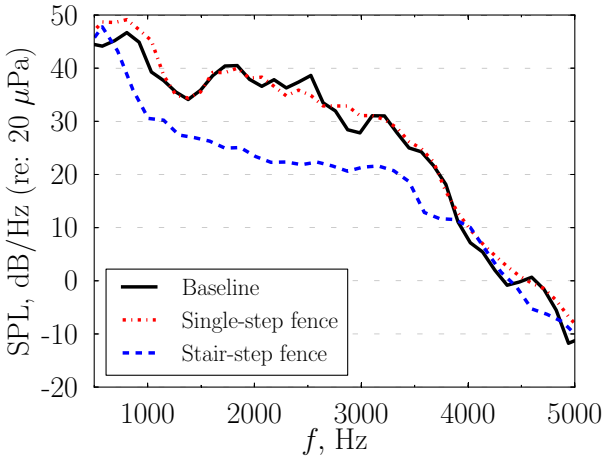

(a) FDL3DI predicted farfield noise spectra

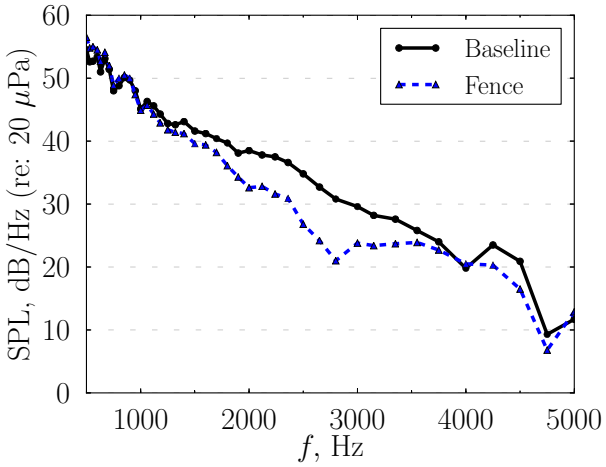

(b) Measured farfield noise spectra

Figure 12. Qualitative comparison between the FDL3DI predicted and measured farfield noise spectra at an observer located at $\theta = 90°$.

The predicted results for the stair-step fence geometry can be compared qualitatively with measured farfield noise spectrum from Ref. [20] shown in Fig. 12b. The measured farfield noise was obtained using beamforming and integrating the one-twelfth octave band spectra over a two-dimensional area near the trailing edge. Although the difference in span lengths between the simulation and experiment is accounted for using Kato's correction [21], due to the difference in baseline airfoil used between the simulations and the experiment, the SPL of the predicted and measured noise cannot be compared. However, the trends for the noise reduction are comparable to the measurements, i.e. little to no noise reduction above 4 kHz and a noise reduction of up to 10 dB between 1 kHz and 4 kHz. Clark *et al.* [20] have suggested that the low frequencies (below 1 kHz) may have a facility noise contribution and hence any potential reduction in noise due to finlets at those frequencies will not be captured by the measurements. Therefore, this may explain the differences in noise reduction with the finlets at frequencies less than 1 kHz.

3.5 Noise Reduction Mechanisms

Two hypotheses are put forth to explain the observed farfield noise reduction with the fence finlets: (1) the fences reduce the spanwise correlation length, and (2) the fences lift the turbulence eddies away from the scattering (airfoil trailing) edge. The second hypothesis is investigated using the simulation results here.

The normalized turbulence kinetic energy (TKE) is obtained by averaging over 2.5τ. The TKE does not significantly change if more than 2.5τ of data is used for the averaging process. Contour plots of normalized turbulence kinetic energy are compared between the baseline and fence simulations at two different cross-stream planes in Fig. 13. The figure shows isometric views with cross-stream cut planes. The first plane at $x/c = 0.85$ is upstream of the fences. At this location, the TKE is concentrated in the boundary layer close to the airfoil surface for all three airfoils. However, at the airfoil trailing edge (see Fig. 13 b, d, & f), the TKE close to the airfoil surface (trailing edge) is substantially reduced with the fences, and appears to be concentrated above the fences. The figure clearly indicates that the separation distance between the source (unsteadiness in the turbulence) and the scattering airfoil trailing edge is increased. Afshari *et al.* [22] conducted an experiment with a similar finlet fence geometry installed over a flat plate at zero incidence. They observed similar trends as seen in the predictions for turbulence intensity (TI); with the fences, the TI decreased near the flat plate and increased above the fences.

Figure 14 compares the span-averaged TKE profiles between the baseline and the fence geometries at the two cross-stream locations corresponding to the plots in Fig. 13. The line plots quantitatively show the reduction in TKE near the surface and concentration of TKE above both the single-step and stair-step fences; the ordinate in Fig. 13 is normalized by the maximum fence height, H. These results substantiate the second hypothesis for the observed reduction in unsteady surface pressure and farfield noise. It is not clear at this time as to why the TKE redistribution with the single-step fences does not result in farfield noise reduction. As hypothesized earlier, the orthogonal leading edge of the single-step fence, which acts as a turbulence (and hence noise) generator, is likely offsetting any benefits gained from the turbulent eddies lifting off the surface.

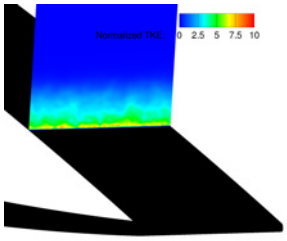

(a) Baseline TKE at $x/c = 0.85$

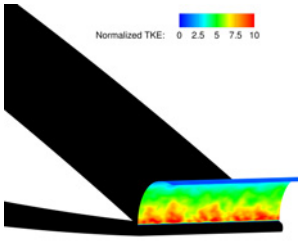

(b) Baseline TKE at $x/c = 0.994$

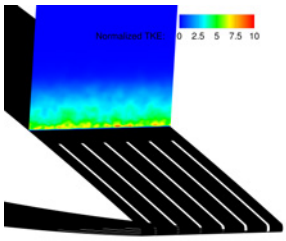

(c) Single-step fence TKE at $x/c = 0.85$

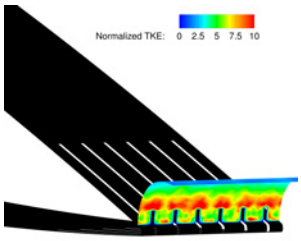

(d) Single-step fence TKE at $x/c = 0.994$

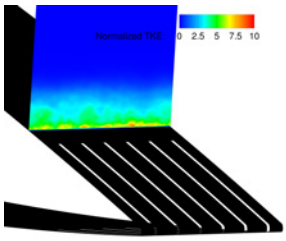

(e) Stair-step fence TKE at $x/c = 0.85$

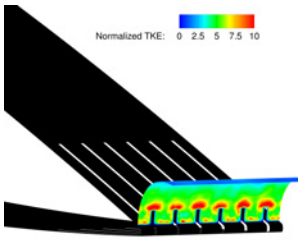

(f) Stair-step fence TKE at $x/c = 0.994$

Figure 13. Normalized turbulent kinetic energy ($k/{u_\tau}^2$) for the baseline and fence simulations: (a, c & e) upstream of the fence at $x/c = 0.85$, and (b, d & f) near the airfoil trailing edge at $x/c = 0.994$.

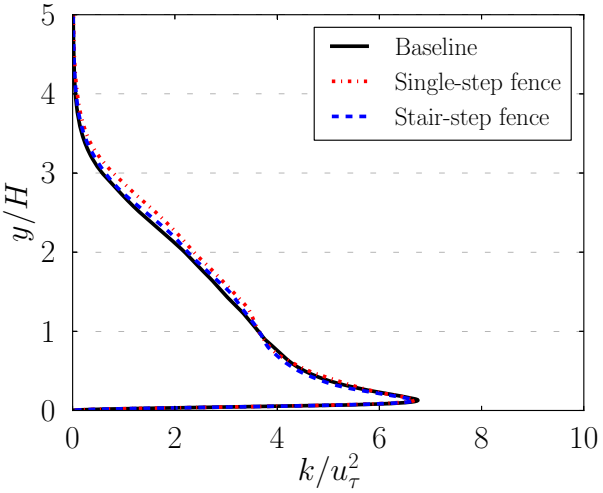

(a) TKE profile at $x/c = 0.85$

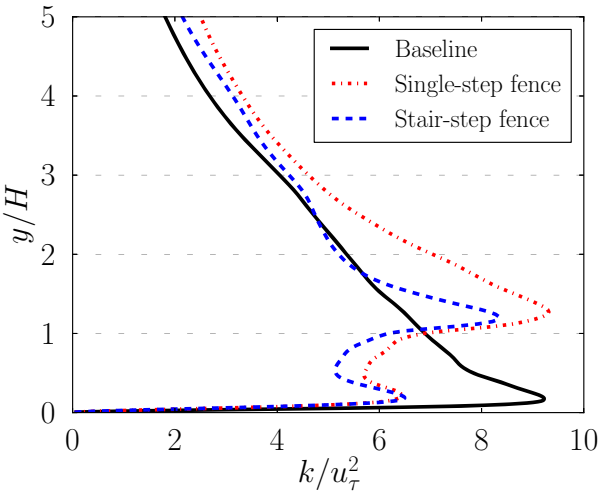

(b) TKE profile at $x/c = 0.994$

Figure 14. Span-averaged normalized turbulent kinetic energy ($k/{u_\tau}^2$) profiles compared between the baseline and fence simulations: (a) upstream of the fence at $x/c = 0.85$, and (b) near the airfoil trailing edge at $x/c = 0.994$.

4. CONCLUSIONS

This paper presents numerical investigations of airfoil geometries inspired by the down coat of the owl. The canopy effect of the down coat is achieved using finlet fences proposed by Clark *et al.* [6]. Large eddy simulations are performed for the baseline (NACA 0012) airfoil and two airfoils with the finlet fences. The following conclusions are drawn from the study:

1. Comparison of surface pressure spectra show a reduction at high frequencies and a slight increase in the low frequencies near the airfoil trailing edge with the fences.

2. Farfield noise spectra show reductions of up to 10 dB at frequencies ranging from 500-5000 Hz for the stair-step fence simulation; no reductions are observed for the single-step fence simulation.

3. Contour plots and span-averaged profiles of normalized turbulence kinetic energy (TKE) show a clear redistribution of TKE away from the airfoil trailing edge.

The results show that one of the reasons for the observed noise reduction with fences is the increased source-scattering edge separation distance, which makes the edge scattering process less efficient. The lack of farfield noise reduction from the single-step fence demonstrates the importance of having a fence leading edge that is highly skewed to the incoming flow.

ACKNOWLEDGMENTS

This research is funded by the National Science Foundation under grant number NSF/ CBET-1554196. Computational resources used for this research are provided by NSF XSEDE

(Grant # TG-CTS130004) and the Argonne Leadership Computing Facility, which is a DOE Office of Science User Facility supported under Contract DE-AC02-06CH11357. Funding through the Wind Energy Science, Engineering, and Policy program is also acknowledged.

REFERENCES

[1] R. D. Sandberg and L. E. Jones. Direct numerical simulations of low reynolds number flow over airfoils with trailing-edge serrations. *Journal of Sound and Vibration*, 330(16):3818–3831, 2011.

[2] Michel Roger, Christophe Schram, and Leandro De Santana. Reduction of airfoil turbulence-impingement noise by means of leading-edge serrations and/or porous material. In *19th AIAA/CEAS Aeroacoustics Conference*. American Institute of Aeronautics and Astronautics, 2013.

[3] Bharat Raj Agrawal and Anupam Sharma. Numerical analysis of aerodynamic noise mitigation via leading edge serrations for a rod–airfoil configuration. *International Journal of Aeroacoustics*, 15(8):734–756, 2016.

[4] Justin W. Jaworski and N. Peake. Aerodynamic noise from a poroelastic edge with implications for the silent flight of owls. *Journal of Fluid Mechanics*, 723:456–479, 2013.

[5] André V. Cavalieri, William R. Wolf, and Justin Jaworski. Acoustic scattering by finite poroelastic plates. In *20th AIAA/CEAS Aeroacoustics Conference*, AIAA Aviation. American Institute of Aeronautics and Astronautics, 2014.

[6] Ian A. Clark, William Devenport, Justin W. Jaworski, Conor Daly, Nigel Peake, and Stewart Glegg. Noise generating and suppressing characteristics of bio-inspired rough surfaces. In *20th AIAA/CEAS Aeroacoustics Meeting*. American Institute of Aeronautics and Astronautics, 2014.

[7] Ian A. Clark, Nathan W. Alexander, William Devenport, Stewart Glegg, Justin W. Jaworski, Conor Daly, and Nigel Peake. Bioinspired trailing-edge noise control. *AIAA Journal*, 55(3):740–754, 2017.

[8] Robert Dougherty. Extensions of DAMAS and benefits and limitations of deconvolution in beamforming. In *11th AIAA/CEAS aeroacoustics conference*, page 2961, 2005.

[9] Andrew Bodling, Bharat Raj Agrawal, Anupam Sharma, Ian A. Clark, Nathan W. Alexander, and William Devenport. Numerical investigations of bio-inspired blade designs to reduce broadband noise in aircraft engines and wind turbines. In *55th AIAA Aerospace Sciences Meeting*. American Institute of Aeronautics and Astronautics, 2017.

[10] Andrew Bodling, Bharat Raj Agrawal, Anupam Sharma, Ian A. Clark, Nathan W. Alexander, and William Devenport. Numerical investigation of bio-inspired blade designs at high reynolds numbers for ultra-quiet aircraft and wind turbines. In *23rd AIAA/CEAS Aeroacoustics Conference*. American Institute of Aeronautics and Astronautics, 2017.

[11] R. Miguel Visbal and V. Datta Gaitonde. On the use of higher-order finite-difference schemes on curvilinear and deforming meshes. *Journal of Computational Physics*, 181(1):155–185, 2002.

[12] J. E. Ffowcs Williams and David L. Hawkings. Sound generation by turbulence and surfaces in arbitrary motion. *Philosophical Transactions of the Royal Society of London. Series A, Mathematical and Physical Sciences*, 264(1151):321–342, 1969.

[13] A. Sharma and H. Chen. Prediction of aerodynamic tonal noise from open rotors. *Journal of Sound and Vibration*, 332(6), 2013.

[14] R. Miguel Visbal. Numerical exploration of flow control for delay of dynamic stall on a pitching airfoil. 32nd AIAA Applied Aerodynamics Conference. American Institute of Aeronautics and Astronautics, 2014.

[15] N. J. Georgiadis, D. P. Rizetta, and C. Fureby. Large-eddy simulation: Current capabilities, recommended practices and future research. *AIAA Journal*, 48(8):1772–1784, 2010.

[16] PEGASUS 5: An automated pre-processor for overset-grid CFD, author=Suhs, E. Norman and Rogers, E. Stuart and Dietz, E. William, booktitle=32nd AIAA fluid dynamics conference, publisher = American Institute of Aeronautics and Astronautics, year=2002.

[17] H. Lee and S. H. Kang. Flow characteristics of transitional boundary layers on an airfoil in wakes. *ASME Journal of Fluids Engineering*, 122:522–532, 2000.

[18] PR Spalart and J. H. Watmuff. Experimental and numerical study of a turbulent boundary layer with pressure gradient. *Journal of Fluid Mechanics*, 249:337–371, 1993.

[19] William R Wolf and Sanjiva K Lele. Trailing edge noise predictions using compressible les and acoustic analogy. In *17th AIAA/CEAS Aeroacoustics Conference*. American Institute of Aeronautics and Astronautics, 2011.

[20] Ian A. Clark, William Devenport, and Nathan W. Alexander. Understanding trailing edge noise control using finlets. *AIAA Journal*, 2017. submitted.

[21] Chisachi Kato and Masahiro Ikegawa. Large eddy simulation of unsteady turbulent wake of a circular cylinder using the finite element method. In *Advances in Numerical Simulation of Turbulent Flows*, volume 1, pages 49–56, 1991.

[22] Abbas Afshari, Mahdi Azarpeyvand, Ali A. Dehghan, and Máté Szőke. Effects of streamwise surface treatments on trailing edge noise reduction. In *23rd AIAA/CEAS Aeroacoustics Conference*. American Institute of Aeronautics and Astronautics, 2017.